npj | computational materials

Article

Published in partnership with the Shanghai Institute of Ceramics of the Chinese Academy of Sciences

https://doi.org/10.1038/s41524-026-02008-x

Dislocation-induced ordering as a source of strengthening in refractory multi-principal element alloys

Yuhao Luo[1,4], Tianyi Wang[1,4], Zhihao Huang[1], Yanqing Su[2], Shuozhi Xu[2], Peter K. Liaw[3] ✉ & Xiang-Guo Li[1] ✉

In refractory multi-principal element alloys (RMPEAs), the rapid atomic diffusion occurring near dislocations facilitates local segregation and chemical ordering, leading to the formation of unique atomic environments capable of pinning dislocations on slip planes. However, previous atomistic simulations have largely overlooked how dislocations induce these unique atomic environments and influence the strengthening mechanism. In this study, we systematically investigate the atomic environments generated by dislocations during annealing and their effects on the mechanical properties of body-centered-cubic (BCC) RMPEAs using hybrid Monte Carlo/molecular dynamics simulations. A machine-learning interatomic potential is specifically trained for these RMPEAs. Our results reveal that the dislocation-core energy, elemental mixing energy, and dislocation-stress field collectively determine unique atomic environments, which strongly pin dislocations and significantly increase the critical resolved shear stress. As the atomic rearrangement near the dislocation core progresses, the enhanced pinning effect of edge dislocations arises from the continuous narrowing of the dislocation-core width, while the increased pinning of screw dislocations is attributed to the dislocation line becoming more kinked. In particular, edge dislocations exhibit a much stronger pinning effect than screw dislocations, consistent with recent experimental results.

As a refractory branch of the multi-principal element alloys (MPEAs) strategy[1,2], refractory MPEAs (RMPEAs) are primarily composed of near-equiatomic, single-phase body-centered-cubic (BCC) solid solutions formed by refractory elements such as Cr, Hf, Mo, Nb, Ta, Ti, V, W, and Zr. In recent years, RMPEAs have attracted significant attention owing to their exceptional resistance to softening at elevated temperatures, making them highly promising for aerospace and chemical industry applications. Numerous RMPEAs with outstanding high-temperature performance have been developed to date[3,4]. For instance, MoNbTaVW and MoNbTaW alloys exhibit remarkable hardness and strength at temperatures up to 1900 K[5]. Nevertheless, the fundamental mechanisms underlying the high strengths of these BCC RMPEAs remain elusive[6]. Increasing evidence suggests that short-range order (SRO) structures could play a crucial role in determining the mechanical properties of RMPEAs[7–10].

In the early days of MPEAs research, it was widely believed that MPEAs were random solid solutions. In contrast, experimental evidence has confirmed that complex interactions among constituent elements often lead to the formation of SRO structures during solidification or heat treatment in alloys such as CoCrNi[11–13], CoNiV[14], MoNbTaW[15], MoNbTaTiZr[16], NbTaTiV[17], and HfNbRuTaZr[18]. Although some studies have questioned the influence of SRO on alloy properties and suggested that its significance may be overstated[19,20], the prevailing consensus is that SRO plays a vital role in determining the mechanical behavior of alloys[12,13,18,21]. Many atomistic simulations have also shown that SRO can induce significant local lattice distortions and directly affect dislocation motion[7,10,22–24]. However, most atomistic studies to date first perform hybrid Monte Carlo (MC)/molecular dynamics (MD) annealing on a perfect crystal to generate SRO, followed by the introduction of dislocations to investigate their interactions with SRO. Since perfect crystals are unlikely to exist during actual annealing, pre-existing defects—such as dislocations—are expected to influence SRO formation. In fact, dislocations may induce unique atomic environments that differ from those formed in perfect crystals during MC processes. These distinctive environments can, in turn, affect dislocations, for example, by causing dynamic strain aging (DSA) and Portevin-Le Chatelier (PLC)[25,26]. For example, experiments based on NbZrTiTa have shown that under high-temperature holding conditions, dislocations can be rapidly locked,

[1]School of Materials, Shenzhen Campus of Sun Yat-sen University, Shenzhen, Guangdong, PR China. [2]School of Aerospace and Mechanical Engineering, University of Oklahoma, Norman, OK, USA. [3]Department of Material Science and Engineering, University of Tennessee, Knoxville, TN, USA. [4]These authors contributed equally: Yuhao Luo, Tianyi Wang. ✉e-mail: pliaw@utk.edu; lixguo@mail.sysu.edu.cn

resulting in an increased peak flow stress[27]. Some related theoretical studies also indicate that, unlike traditional alloys where solute atoms diffuse from remote regions to dislocations, the PLC and DSA effects in MPEAs are associated with the rapid diffusion and rearrangement of atoms near dislocation cores, which may lead to the formation of ordered structures[25,28]. Nevertheless, to the best of our knowledge, most existing simulation studies have largely overlooked the impact of defects on SRO formation. In particular, systematic investigations into how dislocations—as one of the most common types of defects—induce unique atomic environments during annealing, and how these localized inhomogeneous environments influence dislocation motion, remain very limited[26], especially in the context of MPEAs. Figure 1 highlights the distinction between our approach and previous studies. While earlier research has primarily concentrated on the SRO encountered by dislocations during their movement[7,10,23,24], our work focuses directly on the SRO induced by dislocations at the very onset of motion. This induced SRO can strongly pin dislocations. Yet it has been largely overlooked in prior investigations. Addressing this gap is essential for bridging the division between simulations and experiments, and for deepening our understanding of DSA effects and yield phenomena related to dislocation pinning after annealing. Meanwhile, considering that current MPEAs strengthening strategies already leverage the introduction of high dislocation densities to induce precipitation[29,30], it is of great significance for future alloy design to systematically investigate the origins and impacts of dislocation-induced SRO.

On the other hand, to achieve a balance between computational efficiency and accuracy, machine-learning interatomic potentials (ML-IAPs) have been widely adopted in the study of MPEAs[24,31–34]. Previously, Byggmästar et al.[34] and Wang et al.[24] independently developed quinary ML-IAPs for the Mo-Nb-Ta-V-W system. However, as Cr is a common constituent in RMPEAs[35–38], usually added for its excellent corrosion resistance[39], the development of a six-component potential that includes Cr is essential for advancing the understanding and design of high-performance RMPEAs. Currently, there is no ML-IAP available for the six-component Cr-Mo-Nb-Ta-V-W system.

For the above reason, in the current work, we developed a moment tensor potential (MTP) that incorporates the interactions among all six refractory metallic elements: Cr, Mo, Nb, Ta, V, and W. Then, the hybrid MC/MD method is used to simulate the annealing process of alloys. It follows that we investigated the special atomic environments and SRO induced by dislocations during the annealing process, as well as their origins, revealing that the dislocation-core energy, the dislocation-stress field, and the elemental mixing energy jointly determine these special atomic environments. We also investigated the effects of these special atomic environments on mechanical properties and explained their underlying mechanisms. We found that as the MC simulation progresses, the dislocations are strongly pinned, and the critical resolved shear stress (CRSS) increases rapidly. Moreover, the CRSS of a dislocation is directly determined by the atomic configuration of just a few atoms at its core. For edge dislocations, the atomic environment near the core changes, causing the dislocation-core width to shrink and making it more difficult for the dislocation to escape. For screw dislocations, the atomic environment near the core leads to severe spontaneous kinking of the dislocation, which hinders its movement. Amid ongoing debates on the significance of SRO in the mechanical properties of MPEAs[12,19–21], our results underscore the critical role of SRO at the atomic scale.

Notably, our atomistic simulation strategy provides new insights into the mechanisms by which screw and edge dislocations control the strength of BCC RMPEAs. Unlike conventional BCC alloys, recent experimental evidence suggests that, in BCC RMPEAs, edge dislocations contribute to strength control as much as, or even more than, screw dislocations[6,40–42]. While previous simulations have often attributed this feature to a reduced nucleation barrier for kink-pair formation in screw dislocations at high temperatures, thus narrowing the mobility gap between edge and screw dislocations[6,7,43], our results reveal a different perspective: the SRO induced by edge dislocations leads to a much stronger pinning effect than that experienced by screw dislocations, a finding that conventional simulation setups would likely have missed. Furthermore, we found that the atoms at the dislocation core are the primary factor determining the CRSS in MPEAs,

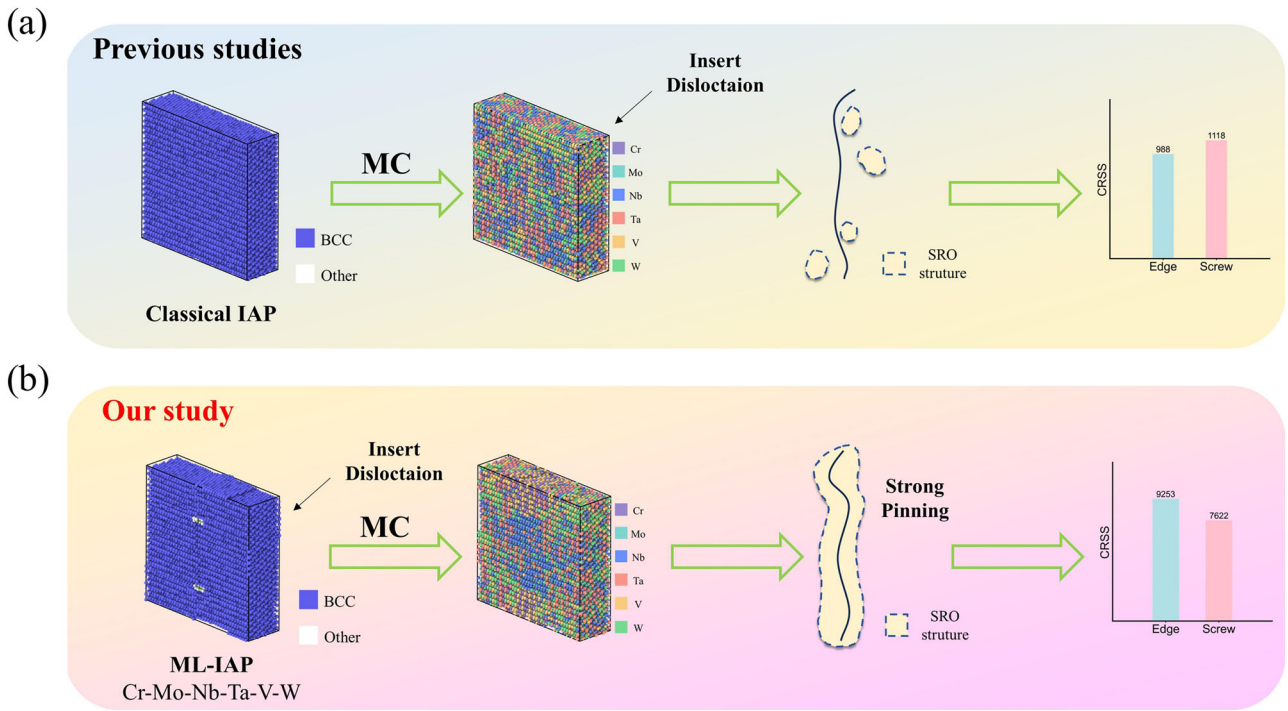

Fig. 1 | The distinction between our approach and previous studies on SRO. **a** Previous research typically began with a perfect crystal, generated SRO through the MC process, and subsequently introduced dislocations to simulate their motion as they traversed SRO regions. **b** Our study starts with a crystal that already contains dislocations, generates dislocation-induced SRO during MC annealing, and then examines how dislocations escape from the unique environments they themselves have created. In contrast to previous studies, our results demonstrate that edge dislocations experience stronger pinning than screw dislocations.

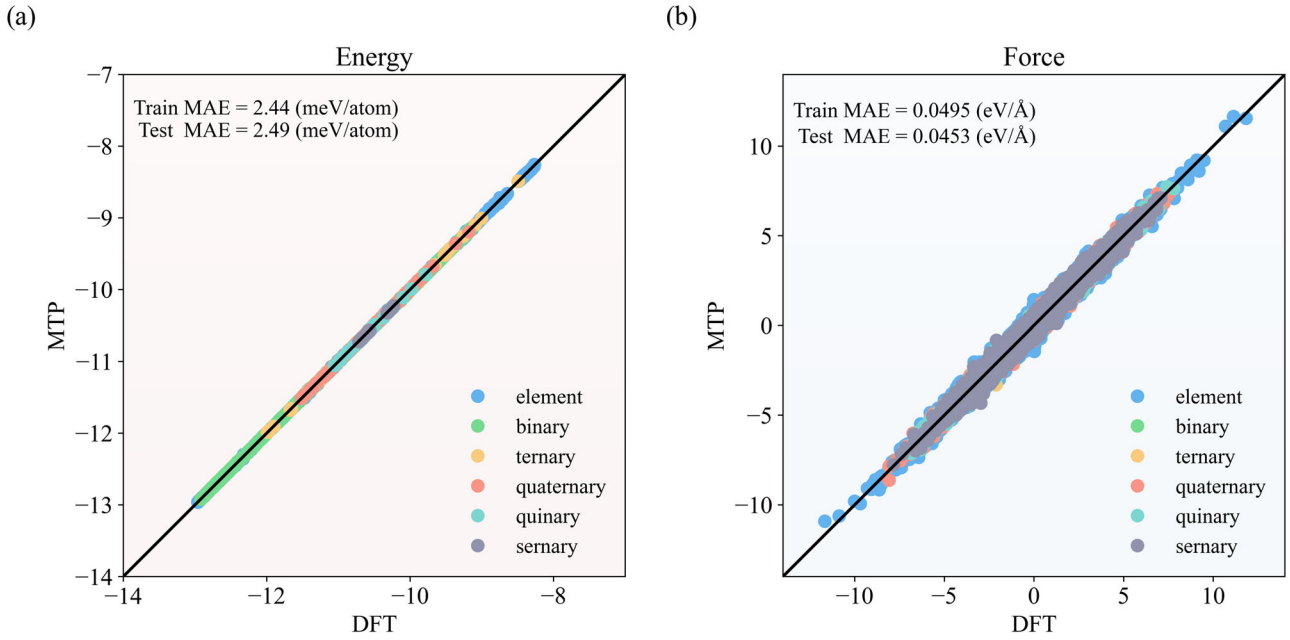

Fig. 2 | Comparison between DFT- and MTP- calculated energies and forces. Systems containing different numbers of elements are marked with various colors. **a** Comparison of energies between DFT and MTP. **b** Comparison of forces between DFT and MTP.

and this finding is consistent with several recently proposed models for the DSA and PLC effects[25,28]. In the discussion section, we will further elaborate on the relevance, consistency, and potential applications of our research in relation to existing experimental studies.

Results

ML-IAP

This section describes the construction of our potential. Among several ML-IAPs, the MTP model was chosen for its favorable balance between computational cost and accuracy[44]. Most of the training and evaluation processes are the same as in our previous work[24], while the training data set has greatly expanded to cover systems that include Cr from unary to senary. Figure 2 shows the comparison of the calculated energy and force of the structures between DFT and MTP in our dataset, and the mean absolute error for both the training and testing set is less than 2.5 meV / atom for energies and 0.05 eV/Å for forces. These results demonstrate the basic accuracy of the MTP model, with neither system exhibiting significantly high errors nor an obvious difference between the errors in the training and testing sets. Additional evaluations of basic properties compared to DFT calculations are provided in the Supplementary Material, including the generalized stacking fault energy (GSFE) (Fig. S1), CRSS (Fig. S2), elastic constants (Table S1), surface energies (Table S2), grain boundary energies (Fig. S3), SRO structures (Fig. S4) and Warren-Cowley Parameter (Fig. S5).

Local chemical environments and their origins

In this section, we focus on the unique atomic environments induced by dislocations and elucidate their underlying mechanisms. Figure 3a, b illustrates that dislocations lead to pronounced local atomic segregation. Figure 3c–e shows the effect of dislocations on the global SRO structure. Using the SRO parameters of a perfect, dislocation-free crystal after the MC simulation as a reference, we find that dislocations, especially edge dislocations, can significantly alter the average global SRO level in RMPEAs. For example, the Cr-V SRO, which is difficult to form in the dislocation-free RMPEAs, emerges in the presence of dislocations. This behavior contrasts with previous reports on CrCoNi medium-entropy alloys[26], where dislocations do not induce notable changes on the global SRO level. Moreover, due to the high-energy state near the dislocation core, only a few MC/MD steps are needed to generate pronounced SRO in the core region. This implies that such SRO is highly likely to exist in real alloys. We will illustrate this point in Fig. S6 of the Supplementary Material.

Next, we examine the differences in local atomic environments induced by dislocations from two perspectives. First, centered on the dislocation, we examine the differences in atomic distributions near the dislocation core. Second, outside the dislocation core, we analyze the differences in the atomic distributions between dislocations.

Firstly, we examine the atomic distributions within the dislocation core. As shown in Fig. 11c, we defined annular cylindrical regions centered on the dislocation line and calculated the atomic concentrations within these regions for different inner and outer radii.

Figure 4a, b present the results after MC simulations (Edge/Screw MC Model), showing a pronounced gradient distribution of elements in the direction perpendicular to the dislocation line. The dashed line indicates the elemental concentration in a fully random system. Both edge and screw dislocations exhibit a consistent trend: regions closer to the dislocation core display higher concentrations of Nb and correspondingly lower concentrations of W. The dislocation-core energies of six pure metals were calculated to explain this phenomenon. The definition of the dislocation-core energy is provided in Section “Atomistic simulations”. As shown in Table 1, both edge and screw dislocations exhibit the highest core energy in W, indicating that more energy is required for W atoms to enter the dislocation core. Consequently, during the MC process, W atoms tend to migrate away from the core region. This trend is consistent with our results in Fig. 4a, b, where the concentration of W decreases near the dislocation and only reaches the elemental concentration in a fully random system at a distance of 8*b* from the core. To support this conclusion, according to the order of dislocation-core energies, the core elemental concentration distributions for the binary alloys, WMo, MoCr, CrTa, TaNb, and NbV, after MC simulations are provided in the Supplementary Material Fig. S7.

However, the dislocation-core energy does not solely determine the elemental distribution near the dislocations. For example, although V has the lowest core energy and would theoretically be expected to have the highest concentration near dislocations, our results show that Nb actually exhibits the highest core concentration. In fact, because of the presence of multiple elements, the mixing energies between elements must also be considered in RMPEAs. The mixing energies of each B2 elemental pair are listed in Table 2 for reference. For example, V–W exhibits a negative mixing energy, indicating a strong tendency for these elements to bond. Although

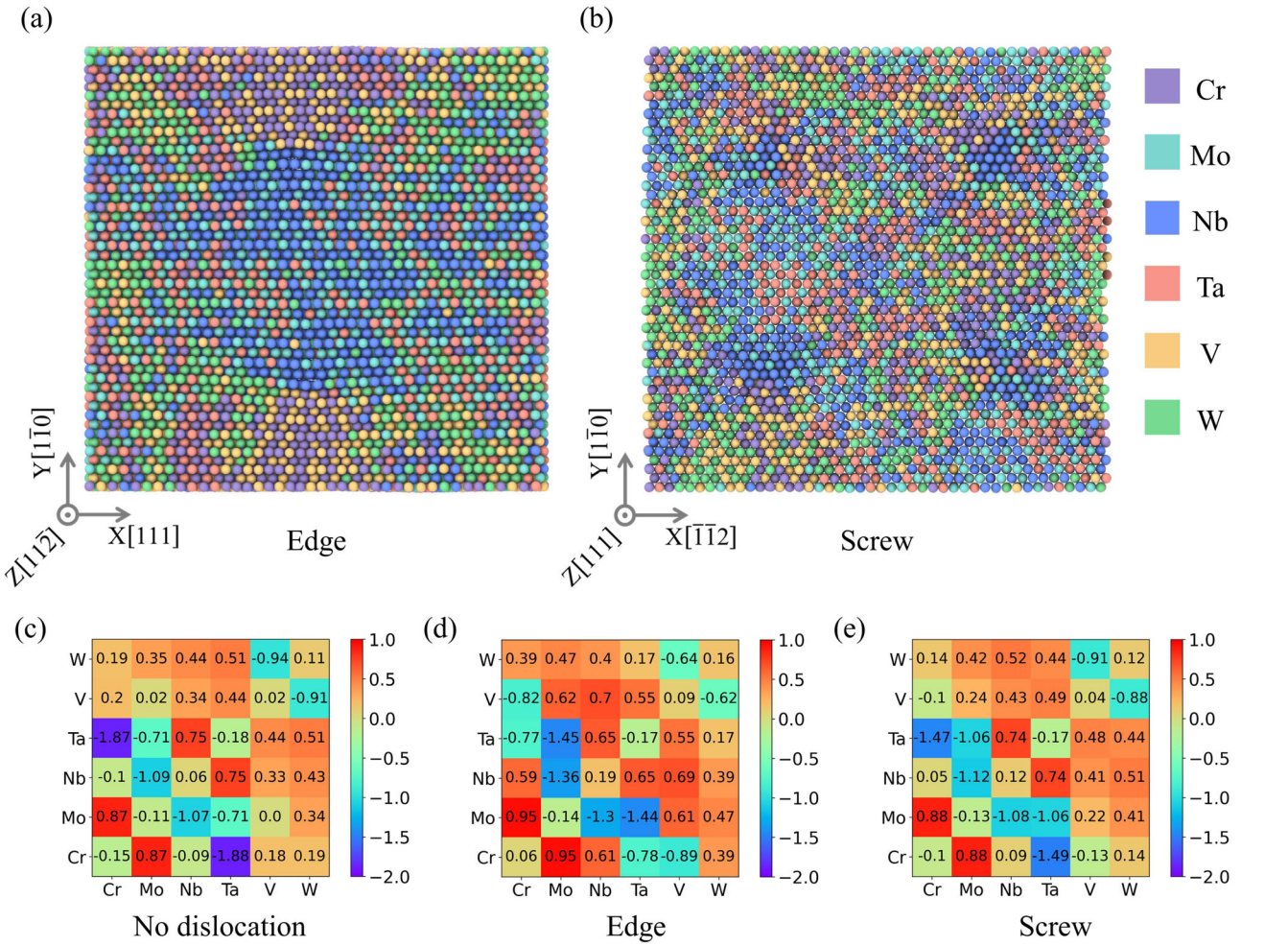

Fig. 3 | Results of the MC/MD simulation for the edge/screw MC model in the CrMoNbTaVW. Snapshots of edge MC (**a**) and screw MC (**b**) models after MC simulations at 300K. Global SRO parameters after MC simulations for models without dislocation (**c**), with edge dislocations (**d**), and with screw dislocations (**e**).

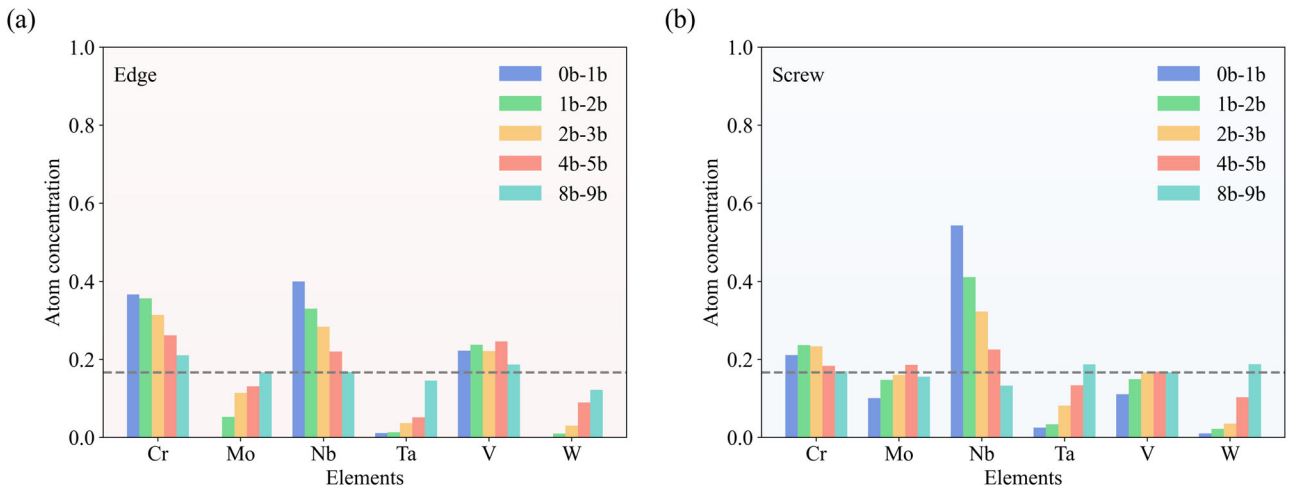

Fig. 4 | Elemental concentration distribution within cylindrical regions near the dislocation core. The gray dashed line represents the elemental concentration in a fully random system. **a** is for the edge dislocation and **b** is for the screw dislocation.

Nb–W also have a negative mixing energy, their bonding tendency is weaker than that of V–W. In fact, the global SRO parameters of a perfect, dislocation-free crystal can be directly used to identify which elemental pairs are favorable or unfavorable for the formation in the alloy. As presented in Fig. 3c, V–V pairs do not exhibit a significant tendency to cluster, V–W pairs show a strong attraction, while Nb-W pairs display a repulsive interaction. Fig. 3d, e demonstrate that V–W bonding is weakened in the presence of dislocation structures. This feature is actually the result of the competition between the dislocation-core energy and the elemental mixing energy. In summary, since (i) W is unfavorable for accumulation at the dislocation core

Table 1 | Dislocation-core energy of pure metals

Element	Edge		Screw	
	E_{core}	r_{core}	E_{core}	r_{core}
W	18.93	3.9	11.90	2.7
Mo	16.65	2.9	9.06	2.5
Cr	10.90	3.3	9.04	3.5
Ta	9.71	4.3	5.37	2.9
Nb	6.41	3.9	4.51	3.7
V	4.90	3.3	3.53	3.3

The unit of E_{core} is eV/nm, and the unit of r_{core} is 1/b.

Table 2 | Elemental mixing energy and lattice constant

Pair	Mixing energy (eV/atom)	a (Å)
CrV	−0.16	2.92
CrMo	0.11	3.02
CrW	0.06	3.03
MoV	−0.25	3.08
VW	−0.16	3.08
CrTa	−0.07	3.10
CrNb	0.10	3.11
NbV	0.11	3.17
TaV	0.05	3.17
MoW	−0.01	3.18
MoNb	−0.23	3.24
MoTa	−0.39	3.24
TaW	−0.21	3.24
NbW	−0.07	3.25
NbTa	0.01	3.32

and (ii) V tends to attract W, and V also becomes unfavorable for aggregation at the core in W-containing alloys. To support this conclusion, MC simulation results for NbV and NbVW alloys are provided in the Supplementary Material Fig. S7 as additional evidence. Additionally, it should be noted that for the atomic distribution at the edge-dislocation core, the dislocation-stress field is also an important factor. In edge dislocations core, the smaller atoms tend to accumulate on the side with the extra half-plane, which explains why elements, such as Cr and V, exhibit higher concentrations in the edge-dislocation model. The effect of the stress field will be discussed in detail later.

Secondly, we investigate the atomic distributions between dislocations, excluding the dislocation core. The presence of a stress field has previously been reported to affect atomic diffusion and rearrangement[45]. Accordingly, under the dislocation-induced stress field, the atomic environments are expected to vary across different stress regions. To demonstrate this feature, we divided the simulation box into 12 layers along the Y-axis or X-axis, and calculated the elemental concentrations, SRO structures, and stress field in each layer. Detailed partitioning methods are provided in Section "Partitioning strategy".

It is well known that the presence of dislocations in a crystal causes surrounding atoms to deviate from their equilibrium positions, resulting in lattice distortion and the formation of an elastic-stress field. According to the elasticity theory, edge dislocations generate both normal- and shear-stress fields, whereas screw dislocations develop only shear-stress fields; see the Supplementary Material, Eqs (1) and (2). In RMPEAs, the stress field becomes more complex due to interactions among different elements and may further evolve during the MC simulation process. In addition, pure shear stresses usually do not cause compression or expansion of the crystal and have little influence on elemental distribution, while the shear stress induced by the BCC screw dislocations can show different effects due to the twinning/antitwinning asymmetry of BCC crystals; As such, we will focus on the normal-stress field for edge dislocations and the shear-stress field for screw dislocations in the following.

For edge dislocations, the initial stress distribution, σ_{xx}, shown in Fig. 5a indicates that the tensile stress is present at the missing atom plane (position B), while the compressive stress occurs at the extra atom plane (position A). Figure 5b presents the stress-field distribution of the edge-dislocation-dipole model at different MC-simulation steps. Specifically, layers 6–7 correspond to the missing atom plane and initially exhibit a tensile stress, whereas layers 12–1 correspond to the extra atom plane and initially present a compressive stress.

Figure 5c reveals that larger elements, such as Nb, Mo, and Ta, move to the tensile regions, while smaller elements, such as V and Cr, migrate to the compressive regions. Similarly, Fig. 5d indicates that B2 structures with larger lattice constants preferentially form in the tensile regions, whereas those with smaller lattice constants form in the compressive regions. The B2 lattice constants for each combination are provided in Table 2. In Fig. 5b, we also observe that as the MC simulation progresses, the degree of SRO increases, gradually reducing the differences between the tensile and compressive stress regions and thereby relaxing the stress. However, with further increases in SRO, the tensile and compressive regions within the dislocation switch positions, and the inhomogeneity in the stress field becomes even more pronounced. The emergence of a reversed stress field may appear counterintuitive. However, from a thermodynamic standpoint, both the relaxation of the stress field and the aggregation of atoms with SRO preferences act to lower the system's energy. In the CrMoNbTaVW system, large atoms such as Mo, Nb, and Ta have a pronounced tendency to cluster, particularly as Mo-Nb and Mo-Ta pairs [Fig. 3c]. As a result, even after the migration of large atoms into the tensile region leads to stress relaxation, continued aggregation of these pairs further reduces the system's energy. Once a substantial number of Mo, Nb, and Ta atoms have already occupied the tensile region, subsequent atoms of the same type preferentially join them, leading to excessive clustering of large atoms. This, in turn, promotes the development of a reversed stress field, converting the original tensile region into a compressive one. Ultimately, the system approaches stability when the energy increase caused by the reversed stress field counterbalances the energy reduction from elemental mixing, resulting in equilibrium between the stress field and elemental distribution. This phenomenon confirms that both the mixing energies of the elements and the stress field jointly influence the distribution of elements in edge dislocations.

For screw dislocations, only a shear-stress field is typically generated. Figure 6a illustrates the distribution of the σ_{xz} shear-stress component, where the position, B, exhibits a significant negative shear stress, corresponding to layers 6–7 in Fig. 6b, while layers 12–1 show a positive shear stress associated with the position, A. Similarly, for the σ_{yz} shear-stress component, positions, C and D, also display shear stresses of opposite signs.

Generally, screw dislocations generate only a shear-stress field and do not induce lattice contraction or expansion. However, a previous study[46] has shown that in BCC crystals, screw dislocations can exhibit a tensile or compressive stress in the direction perpendicular to the {112} plane. This phenomenon arises from a shear/tension coupling associated with the twinning/antitwinning asymmetry of shear on {112} planes. Typically, atomic columns along the [111] direction are offset by $b/3$ relative to each other, with reference positions at $-b/3$, 0, $b/3$, and so on. When the lattice is sheared parallel to a {112} plane, these reference positions shift to $-b/3 - e$, 0, and $b/3 + e$, where e is positive for the twinning shear and negative for the antitwinning shear. As a result, the spacing between neighboring [111] atomic columns increases under twinning shear and decreases under antitwinning shear. Consequently, the lattice tends to be compressed perpendicular to the {112} plane in the twinning case, while it tends to expand in the antitwinning case. More detailed explanations of this phenomenon are provided in the Supplementary Material (Figs. S8, S9, and S10). Therefore, in our screw-

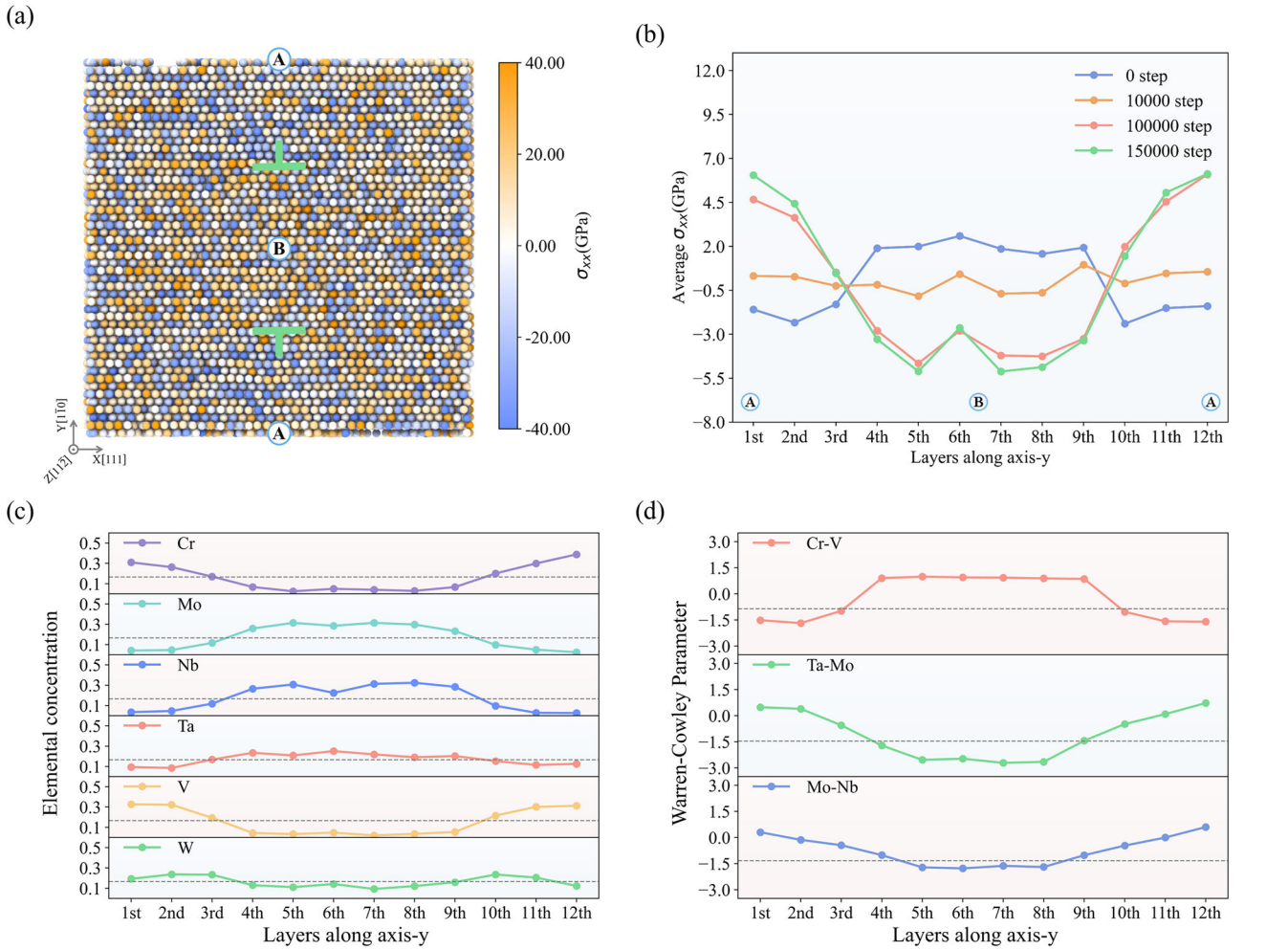

Fig. 5 | Atomic environments induced by the stress field of edge dislocations. **a** Initial σ_x stress distribution of the model prior to the MC simulation. Position A corresponds to the extra half-plane, and position B corresponds to the missing atom plane. **b** σ_x-stress-field distribution along the *Y*-axis after various MC steps. **c** Elemental concentration distributions along the *Y*-axis after the MC simulation. The gray-dashed line represents the global concentration. **d** Distributions of Nb-Mo, Mo-Ta, and Cr-V SRO parameters along the *Y*-axis after the MC simulation. The gray-dashed line represents the global SRO parameter.

dislocation model, the position, B [see Fig. 6a], lies between the antitwinning-shear regions of the two dislocations and is subjected to a tensile stress, while the position, A, lies between the twinning-shear regions and is subjected to a compressive stress. In contrast, positions, C and D, are considered equivalent, as there is no shear asymmetry with respect to the $(1\bar{1}0)$ plane. Figure 6c, d confirm this result. When layering along the *X*-axis, the elemental concentrations and SRO structures at the position, D (layers 6–7) and C (layers 12–1), exhibit no significant differences. However, when layering along the *Y*-axis, the position, B (layers 6–7), is under tension, attracting large-volume elements, such as Nb, and promoting the formation of Mo-Nb atomic pairs with large lattice constants; the position A, (layers 12–1), is under compression, attracting small-volume elements, such as Cr, and favoring the formation of Cr–V atomic pairs with small lattice constants.

In summary, the stress fields generated by both edge and screw dislocations can lead to the aggregation of elements in specific regions. However, the tensile and compressive stresses associated with screw dislocations arise from an asymmetric shear and are much smaller in magnitude than those of edge dislocations, resulting in a considerably weaker effect. Consequently, the changes in global SRO parameters (Fig. 3) induced by screw dislocations are much less pronounced than those caused by edge dislocations.

Impacts on mechanical properties

In the previous sections, we discussed the unique atomic environments induced by edge and screw dislocations in RMPEAs and their underlying mechanisms. In this section, we focus on how these atomic environments affect the mechanical properties of RMPEAs. All data presented here are obtained from the equiatomic CrMoNbTaVW senary.

We first calculate the CRSS of alloys after the MC simulation—including both cases where dislocations were inserted before (Edge/Screw MC Model) and after (MC Edge/Screw Model) the MC simulation—as well as for random alloys (Random Model), to assess the impact of this special atomic environment on alloy strength. Figure 7a shows that the CRSS in the edge/screw MC model is significantly higher than in the MC edge/screw model and the random model. The special atomic environments induced by dislocations increase the CRSS of edge dislocations from about 1 GPa to approximately 9 GPa, and that of screw dislocations to around 7 GPa. Notably, in the edge/screw MC Model, the CRSS of edge dislocations exceeds that of screw dislocations, indicating that the unique environment induced by edge dislocations exerts a stronger pinning effect than that induced by screw dislocations. Figure 7b presents the evolution of lattice distortion during the MC simulation for the edge/screw MC model, with that of the perfect crystal also shown. Compared to screw dislocations, the atomic environment induced by edge dislocations involves greater lattice distortion, further indicating its stronger impact on the system. We also specifically calculate the evolution of the dislocation CRSS in the edge/screw MC model during the MC process. As shown in Fig. 7c, d, at the beginning of the MC simulation, the system energy drops rapidly, and the CRSS increases sharply, reaching plateaus at approximately 20,000 steps. Thereafter,

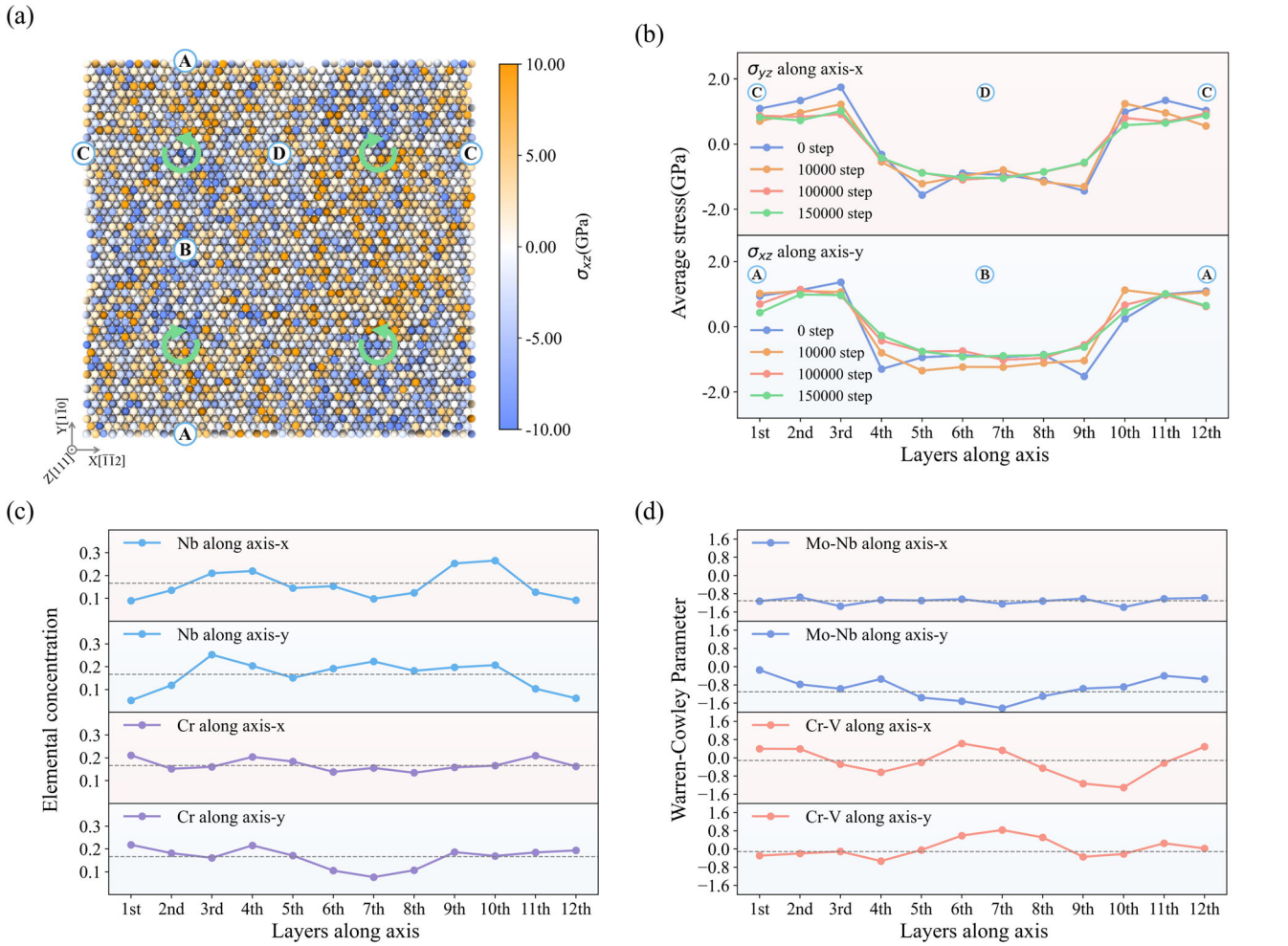

Fig. 6 | Atomic environments induced by the stress field of screw dislocations. **a** Initial σ_{xz} stress distribution of the model prior to the MC simulation. Positions, A, B, C, and D, represent different points between screw dislocations of opposite helicities. **b** Shear-stress-field distribution along the *X*-axis and *Y*-axis at different MC steps. **c** Elemental concentration distributions along the *X*-axis and *Y*-axis after the MC simulation. The gray-dashed line represents the global concentration. **d** Distributions of Nb-Mo and Cr-V SRO parameters along the *X*-axis and *Y*-axis after the MC simulation. The gray-dashed line represents the global SRO parameter.

although the system energy continues to decrease, the CRSS remains nearly constant. In summary, this special atomic environment exerts an influence far beyond that of the conventional SRO, with a more pronounced effect on edge dislocations than the screw ones.

Strengthening mechanisms

To further investigate the origin of the CRSS increase, we retain the core region with a radius of $n \times b$ centered on the dislocation line in the edge/screw MC model, while all atoms outside this region are randomized to form a random alloy. For details, see Section "Atomistic simulations". As shown in Table 3, when atoms within a radius of 3*b* are retained, the CRSS of the dislocation remains close to its original value. Even when only atoms within a smaller radius are selected, a certain degree of strengthening is still observed. This feature indicates that the increase in CRSS is primarily due to a very small fraction of special atomic environments near the core formed during the MC process. In other words, after the MC simulation, both edge and screw dislocations are pinned by a small number of atoms in the core region. Notably, even fewer atoms are required to pin edge dislocations compared to screw dislocations.

Indeed, changes in the atomic environment provide indirect evidence for this conclusion. As shown in Fig. 8, using the method illustrated in Fig. 11c, we analyze the evolution of elemental concentrations near the dislocation during the MC simulation and find that concentrations within the 0–2*b* range become essentially stable after 20,000 simulation steps. This stabilization coincides with the rapid increase and subsequent plateau of the CRSS at around 20,000 steps. In contrast, elemental concentrations in the 2*b*–4*b* range remain far from being stable at 20,000 steps, yet their subsequent changes have little impact on the CRSS. This trend suggests that the pinning effect on the dislocation is primarily determined by the atomic environment in the immediate core region, while changes further away have a negligible effect. Therefore, we will next focus on the structural changes of dislocations in the core region.

For edge dislocations, our previous analysis has shown that their strength is primarily determined by a very small number of atoms near the core. According to the Peierls-Nabarro model, the strength of a dislocation is highly sensitive to a change in the core width[47]. Therefore, we analyze the evolution of the dislocation-core width and CRSS during the MC process for RMPEA alloys. Figure 9a presents the extraction of the disregistry from the dislocation slip plane and the calculation of the misfit density. The definition and calculation of the core width are detailed in Section "Atomistic simulations". Figure 9b exhibits the misfit density calculated for the CrMoNbTaVW at different MC steps. A sharper peak in the misfit density indicates a narrower dislocation core. We observe that before 20,000 steps, the dislocation core becomes narrower, while after 20,000 steps, the core width changes very little. To assess the transferability of our findings, we repeat the simulation in two other alloys, WTaVCr and MoNbTaVW, as shown in Fig. 9c. Remarkably, we found that the six-, five-, and four-component alloys all exhibit similar strong pinning effects after MC simulations with edge

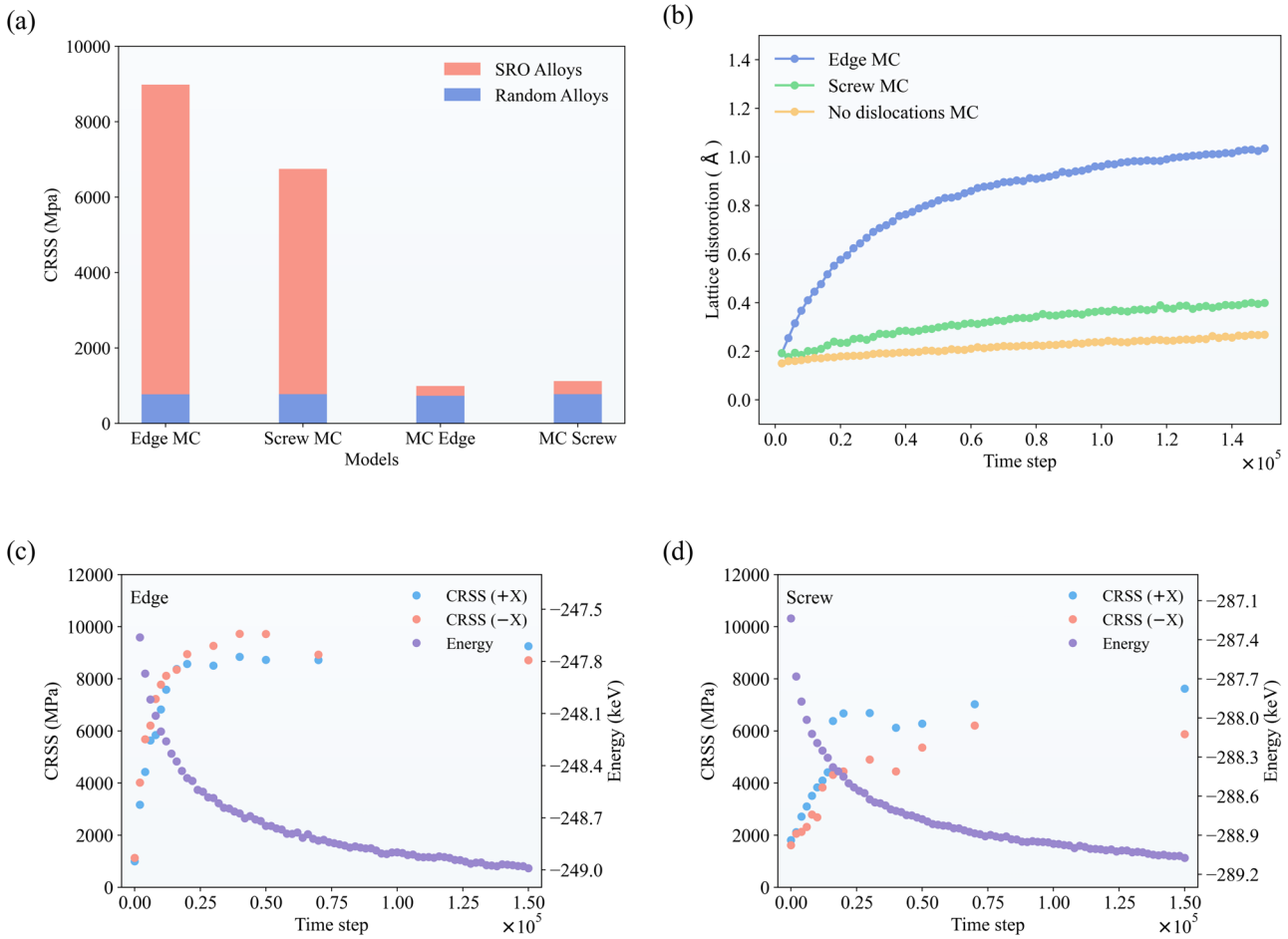

Fig. 7 | Effect of special atomic environments induced by dislocations on CRSS. All data are from the CrMoNbTaVW. **a** Average CRSS in different models. **b** Lattice distortion in various models. **c**, **d** Variation of CRSS with MC-simulation steps in edge/screw MC models. $+X$ and $-X$ represent applying strains along the positive and negative directions of the X axis, respectively.

dislocations, despite significant differences in the elemental composition at the dislocation cores. In Fig. 9d, by comparing the normalized dislocation-core width and CRSS, we found that they exhibit an approximately negative exponential relationship, consistent with the classical theory. In all three alloys, the dislocation-core width is very small, not exceeding b. As previously discussed, the atomic environment within $2b$ of the dislocation core stabilizes after 20,000 simulation steps. Since atoms near the core primarily determine the core width, the dislocation-core width no longer decreases after 20,000 steps, resulting in the CRSS converging to a high value.

For screw dislocations, previous studies have shown that they can spontaneously form kinks in MPEAs even without thermal activation[48]. Unlike edge dislocations, which always maintain their configuration to minimize the line tension throughout the MC process[26], the bending of screw dislocations is actually an adaptation to the surrounding atomic environment, thereby reducing the dislocation energy. Therefore, we believe that the bending of screw dislocations actually reduces the system energy, leading to their pinning. Here, we use the waviness parameter to quantify the degree of bending of screw dislocations (see Section "Atomistic simulations" for details). Figure 10a shows the evolution of the waviness parameter for the screw dislocation in the CrMoNbTaVW model during the MC simulation, indicating that the degree of kinking increases as the simulation progresses. Moreover, evidence presented in the Supplementary Material Fig. S11 demonstrates that the evolution of the waviness parameter during the MC process indicates that edge dislocations remain nearly straight. As shown in Fig. 10b, we perform MC simulations with dislocations in all three alloys and track the evolution of CRSS throughout the MC process. Although similar pinning trends are observed across the different alloys, the pinning strength varies significantly. Figure 10c further demonstrates that the CRSS of screw dislocations is proportional to their waviness. Among the three alloys, the screw dislocations in the CrMoNbTaVW exhibits the greatest degree of bending and, consequently, the highest CRSS. In addition, as listed in Table 3, the greater bending of screw dislocations—compared to edge dislocations—results in a larger core region influenced by the dislocation, thereby involving more atoms in determining their strength. It is also worth noting that in the screw-dislocation model discussed earlier, the dislocation length is about 3.3 nm. By shortening the model length along the dislocation line to 1.65 nm, we artificially reduced the possibility of kinking during the MC process, and found that the pinning strength in screw dislocation is significantly lower than that of the 3.3 nm dislocations. However, further increasing the dislocation line length to 6.6 nm does not lead to a noticeable enhancement in pinning strength (see Figs. S12 and S13 of the Supplementary Material). In fact, while the dislocation tends to bend to adapt to local low-energy environments, this bending also increases the overall line length (and thus the energy, as a longer line corresponds to higher energy). The maximum degree of bending that a dislocation can achieve is determined by the balance between these two factors. Therefore, except in extremely short dislocation models, the length of the model has a limited effect on dislocation bending. As such, the results obtained with the 3.3 nm model can reliably represent the behavior of longer and even real dislocations.

Discussion

In the present work, we systematically investigate the strengthening mechanisms in RMPEAs by analyzing the atomic environments induced by

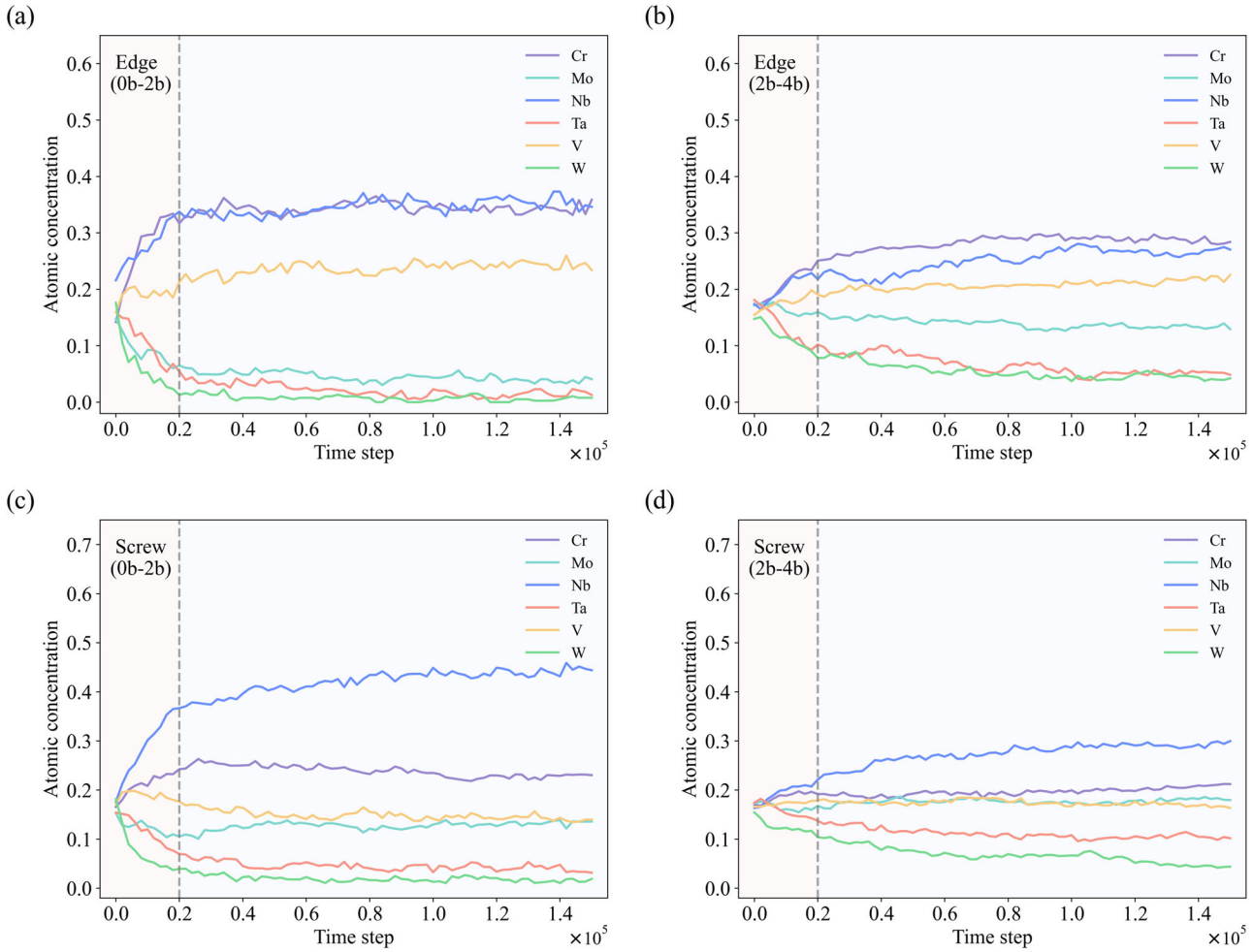

Fig. 8 | Evolution of elemental concentrations in edge/screw-dislocation cores during MC simulations. The gray-dashed line represents 20,000 time steps. The method for region partitioning is described in Section "Partitioning strategy". **a**, **b** Elemental concentrations in the 0*b*--2*b* and 2*b*--4*b* regions of the edge-dislocation model. **c**, **d** Elemental concentrations in the 0*b*--2*b* and 2*b*--4*b* regions of the screw-dislocation model.

Table 3 | CRSS calculated after randomly shuffling atoms outside the core region

	CRSS (MPa)	
Core region size	**Edge**	**Screw**
b	5825 ± 313	4634 ± 40
2*b*	8263 ± 206	5900 ± 196
3*b*	9027 ± 99	6557 ± 208
4*b*	8732 ± 238	7095 ± 21
Original values	9253	7622

Each model is calculated 3 times. The unit is MPa. All data is obtained from the equiatomic CrMoNbTaVW senary alloy.

dislocations and their impacts on mechanical properties. MC simulations reveal that the atomic environment and the core structure near the dislocation core play a dominant role in determining the CRSS.

Our results show that the dislocation-core energy of elements, the elemental mixing energy, and the dislocation-stress field collectively determine the unique atomic environment induced by dislocations. Since these three factors intertwine and compete with each other, it is difficult to separate them for quantitative analysis. For regions in the dislocation core, we can only qualitatively identify which elements are likely to migrate into the dislocation-core region and which are likely to be expelled. For regions outside the dislocation core, the elemental distribution around edge dislocations is primarily governed by the presence of missing or extra half-planes. Notably, for screw dislocations, our results reveal both symmetric and asymmetric configurations along different orientations. This phenomenon is closely linked to the intrinsic asymmetry of the {112} planes in BCC structures.

In particular, given the significance of elemental distribution at the dislocation core revealed by our study, the ability to predict dislocation-induced SRO at the core for various alloy compositions would significantly advance our understanding of alloy behavior. Currently, we can only make a simple assessment based on the dislocation-core energy of each element. For more accurate predictions, a promising strategy is to systematically explore combinations of different elements to generate a diverse set of alloy compositions, then calculate the elemental distribution at the dislocation core for each case and quantify the influencing factors, and use this data to train a predictive model.

It is also important to clarify that the ordered structures identified in our study are derived from MC/MD simulations, which primarily consider thermodynamic aspects. In MPEAs, atomic diffusion is generally quite slow. However, theoretical studies have shown that atomic diffusion and local rearrangement rates near dislocation cores in MPEAs are exceptionally high—even moving dislocations during deformation allow sufficient time for such rearrangements to occur[25,28]. Therefore, in our research, the role of kinetics can be simply considered as follows: the closer to the dislocation core, the more the SRO observed in real MPEAs will resemble our

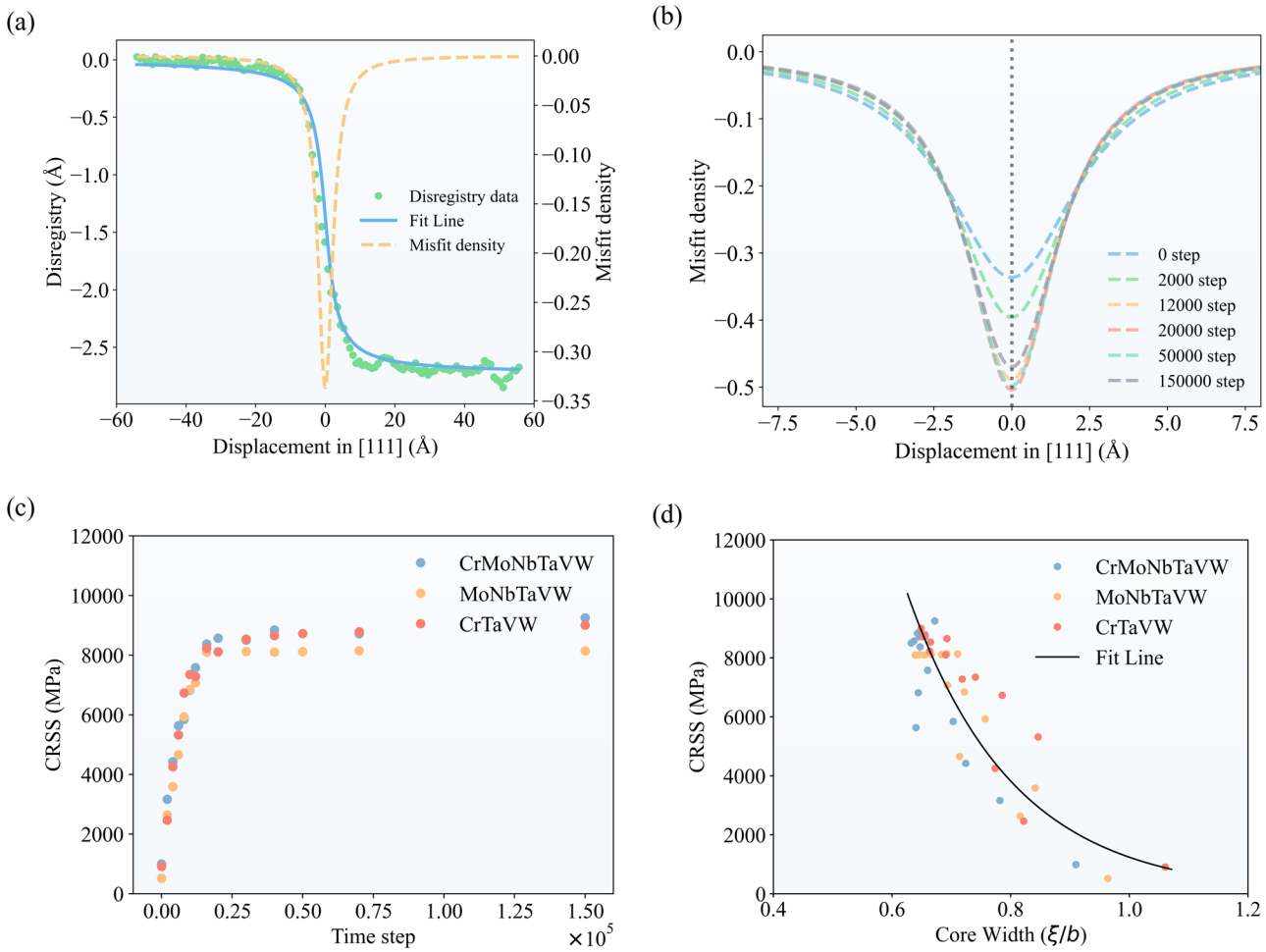

Fig. 9 | Edge-dislocation core and CRSS evolution during MC simulations. **a** Distribution of disregistry (blue line) and misfit density (yellow line) around the edge-dislocation core along the [111] direction at the initial MC step in the CrMoNbTaVW alloy. **b** Misfit density of the CrMoNbTaVW alloy at various MC steps. **c** Evolution of the CRSS for the three alloys in the edge MC model throughout the MC simulation. **d** Relationship between the CRSS and the corresponding normalized dislocation-core width.

thermodynamic simulation results; farther away from the core, SRO may be more difficult to observe due to kinetic limitations. In contrast, SRO in perfect crystals is expected to be weaker, which may also be one of the challenges in directly observing SRO experimentally.

Further simulations indicate that the atomic behavior in the core region exerts a strong pinning effect on dislocations, which majorly determines the CRSS value. The process by which a dislocation escapes from a strong pinning point is intimately associated with the yielding phenomenon of the alloy. Therefore, we focus on the process of a dislocation escaping from the unique atomic environment that it induces.

For edge dislocations, the core width is fundamentally determined by the balance between the misfit energy and the elastic-strain energy induced by the dislocation. In our model, we observe that during the MC simulation, the dislocation-core width decreases rapidly and then stabilizes, with occasional slight relaxation. We reason that when low-modulus elements, such as Nb, enter the dislocation core, they are compressed by the surrounding alloy, causing the core to contract. As the atomic environment in the core region gradually stabilizes, the core width also becomes stable. Additionally, excessive local aggregation of Nb may reduce the unstable stacking fault energy, resulting in the slight relaxation of the dislocation core.

For screw dislocations, we believe that kinking is an adaptation to the surrounding atomic environment that lowers the system energy. The greater the degree of kinking, the deeper the dislocation is trapped in a low-energy potential well, making it more difficult to escape. Additionally, the bending of screw dislocations on non-slip planes further impedes their motion to some extent. For shorter screw dislocations (less than 1.65nm), significant kinking is unlikely to occur during the MC process, resulting in a lower CRSS compared to screw dislocations with greater kinking, though still higher than that of screw dislocations in the conventional SRO model, in which the dislocation is inserted after the MC run. This trend may suggest that, beyond the strengthening effect from kinking, there exists a more intrinsic strengthening mechanism.

Our simulations offer atomic-scale insights into the strengthening mechanisms of MPEAs and hold great potential for further narrowing the gap between experimental observations and theoretical modeling. In the following, we present recent experimental findings on dislocation behavior in MPEAs and discuss the applicability of our simulation approach to related research, as well as the consistency of our conclusions with experimental results at the atomic scale. Furthermore, we discuss some alloy design strategies in MPEAs based on dislocation-induced ordering structures.

Recent studies on MPEAs have identified a temperature regime in which the strain hardening exponent increases with increasing temperature —a counterintuitive trend attributed to the DSA effect[49]. In contrast to conventional alloys, MPEAs display a distinctive PLC effect that evolves with the number and type of constituent elements, and the additional strengthening resulting from DSA is even more pronounced[25]. It is foreseeable that our developed ML-IAP and simulation models can be readily and efficiently extended to related systems, offering valuable insights. Notably, new theoretical models have been proposed for the PLC effect in

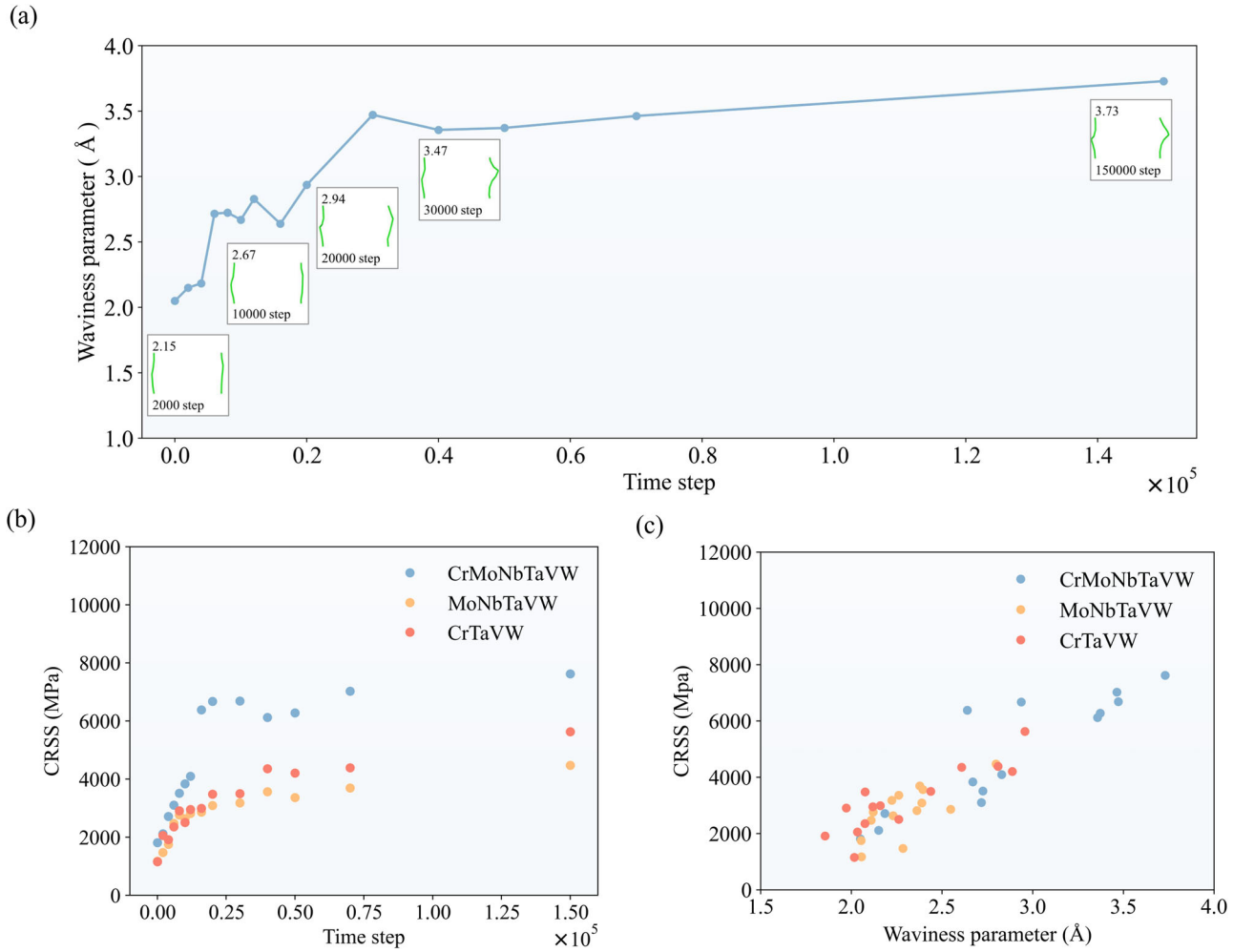

Fig. 10 | Screw-dislocation waviness and CRSS evolution during MC simulations. **a** Evolution of the waviness parameter for the screw dislocations during the MC simulation in the CrMoNbTaVW alloy. Representative snapshots of a pair of dislocations at selected MC steps are also shown. **b** Evolution of the CRSS for the three alloys in the screw MC model throughout the MC simulation. **c** Relationship between the CRSS and the corresponding waviness parameter.

MPEAs[25,28]. In these models, unlike in traditional alloys, solute atoms do not migrate from distant regions to the dislocation core; rather, atoms in the vicinity of the dislocation core rapidly rearrange, frequently reducing the dislocation energy and leading to temporary pinning—thus producing the PLC effect. Consistent with this, our simulations demonstrate that the atomic configuration at the dislocation core almost directly determines the CRSS, and that these core atoms quickly stabilize during the MC process.

Meanwhile, recent experimental studies on BCC RMPEAs have shown that edge dislocations can overwhelmingly dominate the plastic deformation process at room temperature[42]. Additionally, it has been reported that, in the CrMoNbV[42] and the TiZrHfNbTa[41], the dominant dislocation type may transition from edge to screw during deformation. Specifically, edge dislocations are predominant in the initial stage, while screw dislocations gradually take over as deformation progresses[41]. Intriguingly, our simulations provide an atomic-scale explanation for these observations. We find that, after annealing, edge dislocations experience significantly stronger pinning than screw dislocations due to dislocation-induced SRO structures. This strong pinning effect causes edge dislocations to dominate in the early stages of deformation, and as the deformation proceeds, edge dislocations may gradually escape from these pinning sites, allowing screw dislocations to emerge as the main carriers of plasticity. In contrast to previous interpretations that attributed the dominance of edge dislocations at high temperatures to differences in the temperature sensitivity of slip resistance, our findings underscore the critical and distinctive role of SRO-induced pinning in governing the various stages of plastic deformation.

Lastly, it is noteworthy that recent studies have employed metal-based 3D printing techniques to fabricate MPEAs with intrinsically high dislocation densities[29,30]. Upon annealing, these alloys evolve into a dislocation-precipitate skeleton, thereby enabling a synergistic strengthening mechanism that combines both dislocation and precipitation hardening. This strategy achieves significant improvements in the strength of MPEAs without compromising their ductility. Such findings underscore the critical role of dislocation-induced ordered structures in governing the mechanical properties of MPEAs. Our research contributes to a deeper understanding of the origin, composition, and influence of these dislocation-induced ordered structures, offering valuable insights for the rational design of next-generation MPEAs.

In conclusion, this study elucidates the strengthening mechanisms of RMPEAs at the atomic scale. We developed a new ML-IAP for this senary system and, by inserting dislocations prior to MC annealing, more realistically captured the evolution of SRO and local atomic environments in the presence of dislocations, thereby narrowing the gap between experiments and simulations. Our analysis shows that dislocation-induced atomic environments are governed jointly by dislocation-core energies, elemental mixing energies, and the dislocation-stress field, and that the atomic structure near the core critically determines the CRSS: for edge dislocations, the core width is the dominant factor, whereas for screw dislocations the degree of kinking contributes significantly to strengthening. The simulation framework helps to rationalize multiple experimental observations and provides practical guidance for predicting dislocation-induced SRO,

Table 4 | Models used for CRSS calculation

SRO Alloy	
Edge/screw MC model	Dislocations were inserted before performing MC simulations. (Screw dislocations are inserted in the form of quadrupoles, and edge dislocations are inserted in the form of dipoles. Other models all follow the same dislocation pattern.)
MC edge/screw model	MC simulations were performed on the perfect crystal, followed by the insertion of edge-dislocation dipoles or screw-dislocation quadrupoles. (The CRSS calculation was repeated 16 times by inserting dislocations at different positions.)
***n* × *b* model**	Selected the edge/screw MC model in which dislocations had been inserted, and the MC simulation was complete. A cylinder of a radius, $n \times b$, was constructed and centered on the dislocation line, and only the atoms within this cylinder were retained. For atoms outside the cylinder, their elemental types were randomly reshuffled to eliminate SRO structural features in these regions, thereby allowing the analysis to focus on the effects of the dislocation core and its surrounding atoms. Here, b is the magnitude of the Burgers vector of the material, and n is the multiple of b used to define the cylinder radius.
Random alloy	
Random model	Edge-dislocation dipoles or screw-dislocation quadrupoles were inserted into the model with random elemental distributions. (16 different structures were calculated for each alloy.)

optimizing processing/annealing routes, and designing next-generation RMPEAs.

Methods

ML-IAP

Our ML-IAP is constructed using the MTP framework[50]. In this approach, the total energy is expressed as the sum of contributions from all atoms, with the potential energy of each atom determined by its neighboring atomic environment:

$$E = \sum_i V_i(u_i) \tag{1}$$

where u_i denotes the coordinates of neighboring atoms within the spherical shell surrounding atom i. The number of atoms considered around the central atom is determined by the cut-off radius R_c. V_i is expressed as a linear combination of a set of basis functions $B_l(R_i)$ and parameters θ_l:

$$V_i = \sum_{l=1}^{m} \theta_l B_l(R_i) \tag{2}$$

where the number of functions, m, is selected to balance the accuracy and computational efficiency. The basis functions $B(R)$ are constructed by contracting a set of moment tensors to a scalar, and the moment tensors are defined as follows:

$$M_{\mu,\nu}(R) = \sum_j f_\mu R_{ij} \bigotimes \ldots \bigotimes R_{ij} \tag{3}$$

where f_μ represents the radial distribution of the neighboring environment around an atom, i, and these functions are specified according to the atomic type of the neighboring atom, j. $R_{ij}\bigotimes \ldots \bigotimes R_{ij}$ are tensors of the rank, v, including the angular information about the atomic environment. The moment tensors, serving as descriptors of the neighboring environment, are contracted to be rotationally invariant, and the basis functions satisfy all relevant physical symmetries.

Training data

To accurately capture the interactions among six elements, a large and diverse dataset is required. However, an excessive amount of data may result in overfitting. The data categories used for training our potential are selected based on our previous successful work on binary[31], quaternary[32], and quinary[24] alloys, which effectively describe dislocation-related properties. During the training process, we iteratively alternate between fitting and validation, manually adjusting the weights of different data types to achieve optimal potential performance. The final optimized training dataset covers all combinations from unary to senary systems. A detailed description of the training data is provided below:

For elemental systems, snapshots were obtained from ab initio molecular dynamics (AIMD) NVT simulations of a 3 × 3 × 3 bulk supercell at 300, 1000, and 3000 K, with additional AIMD NVT simulations at 300 K performed at 90% and 110% of the equilibrium 0 K volume. Snapshots were recorded every 0.1 ps, yielding 200 snapshots per element. Surface structures were generated for all surfaces with Miller indices less than 3. Conventional cell structures under strain, including the ground-state configurations, were created with strains from −10% to 10% in 1% increments for six different deformation modes[51].

For binary systems, A_xB_{1-x} solid-solution structures with randomly distributed atoms were constructed within a 2 × 2 × 2 supercell for compositions x ranging from 0 to 100 at% in increments of 6.25 at%.

For ternary, quaternary, quinary, and senary systems, special quasi-random structures (SQSs)[52] were generated using the ATAT code[53] in 3 × 3 × 3, 4 × 4 × 4, and 5 × 5 × 5 supercells, respectively. Both relaxed and unrelaxed configurations and snapshots captured during structural optimization were included to improve force prediction, and additional snapshots were collected from AIMD NVT simulations of these SQSs at 300, 1000, and 3000 K.

Atomistic simulations

Using atomsk[54], we insert an edge dipole or a screw quadrupole in a system with a random atomic distribution. The reason why a screw dipole is not used is because it is less stable than a quadrupole. In the present work, we only investigate dislocations for the 1/2⟨111⟩{110} slip system. The reasons for our choice of the dipole/quadrupole model and the relatively short dislocation line length is provided in the Supplementary Material. The edge-dislocation model is a $11 \times 11 \times 3.3$ nm^3 cell, using the slip direction, [111], as the X-axis, the slip plane normal, $[1\bar{1}0]$, as the Y-axis, and the dislocation line direction, $[11\bar{2}]$, as the Z-axis. The screw-dislocation model is a $11.5 \times 11.5 \times 3.3$ nm^3 cell, using the slip direction, $[\bar{1}\bar{1}2]$, as the X-axis, the slip plane normal, $[1\bar{1}0]$, as the Y-axis, and the dislocation line direction, [111], as the Z-axis. Each cell was then relaxed to a physically reasonable configuration. All atomistic simulations in this paper were performed using Large-scale Atomic/Molecular Massively (LAMMPS)[55] with the newly developed ML-IAP. Three equiatomic RMPEAs—CrMoNbTaVW, MoNbTaVW, and CrTaVW—are considered. In what follows, we present the specific parameter settings and calculation methods.

Hybrid MC/MD. For each type of RMPEAs, we build an edge-dislocation model, a screw-dislocation model, and a corresponding dislocation-free model. The system initially has a random atomic distribution with periodic boundary conditions applied along all three directions. It follows that a hybrid MC/MD simulation is performed at 300 K, while an MC swap between different species is performed only once in each MD step. The structure is exported every 2000 MD steps for subsequent calculations.

CRSS. The CRSS is calculated at 0 K using the molecular statics (MS) method. Periodic boundary conditions are applied along the dislocation line (Z direction) and the slip direction (X direction), while the direction

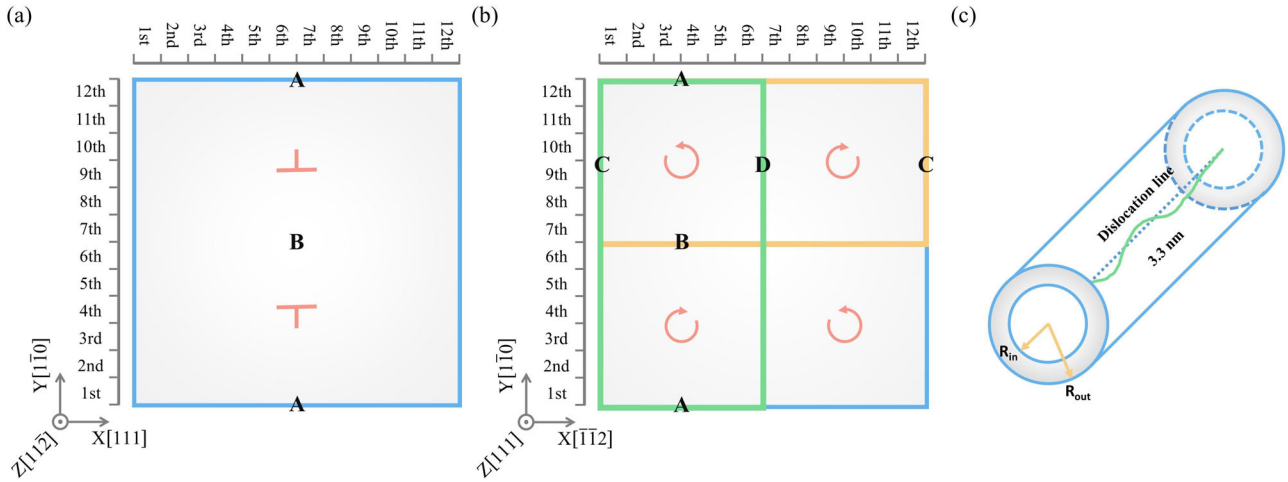

Fig. 11 | Schematic of the dislocation models and the layering strategy along the *X* and *Y* axes. a Edge-dislocation-dipole model. Position, A, corresponds to the extra half-plane, and position, B, represents the missing atom plane. **b** Screw-dislocation-quadrupole model. Positions, A, B, C, and D, represent different points between screw dislocations of opposite helicities. The yellow box indicates the region considered when layering along the *X*-axis, and the green box indicates the region considered when layering along the *Y*-axis. **c** Schematic of the cylindrical region near the dislocation core, where R_{out} is the outer radius and R_{in} is the inner radius.

perpendicular to the slip plane (*Y* direction) is set as non-periodic. A displacement-controlled loading mode is employed[56], with the top and bottom boundaries in the *Y* direction fixed and then subjected to displacement. The same strain increment of 8×10^{-5} is applied to both screw and edge-dislocation models. The various models used for CRSS calculations are summarized in Table 4.

Dislocation-core energy. The total strain energy per unit length of a dislocation within a region can be calculated using the following equation:

$$E_{\text{total}}(r) = \frac{1}{L_{\text{d}}}[E_{\text{system}}(r) - NE_{\text{cohesive}}] \tag{4}$$

where L_{d} is the length of the dislocation line, $E_{\text{system}}(r)$ is the total energy of the cylinder with radius, *r*, and E_{cohesive} is the cohesive energy. According to previous studies[57,58], the dislocation-core radius is defined as the point where E_{total}-ln*r* begins to deviate from the linear relationship. E_{core} is defined as the total energy at r_{c}.

Dislocation-core width. Since our models use edge-dislocation dipoles, there are non-negligible interactions between dislocations. In addition, due to the presence of multiple elements in RMPEAs, it is challenging to directly estimate the dislocation-core size using the methods for calculating the dislocation-core energy in pure metals. Therefore, we use the Peierls–Nabarro (P–N) model to characterize the dislocation core spreading over a finite region along the slip plane. The discrepancy between the two misfit blocks follows the function as

$$u(x) = (b/\pi)\arctan(x/\zeta) + b/2 \tag{5}$$

where ξ is the half-width of the edge-dislocation core. We directly extract the disregistry $u(x)$ from the core structure to calculate ξ, thereby providing a more accurate description of the dislocation core's evolution during the MC-simulation process.

Lattice distortion. Here, we use the root mean square atomic displacement to represent lattice distortion,

$$d = \sqrt{\frac{1}{N}\sum_{i=1}^{N}(r_i - r_i^{ideal})^2} \tag{6}$$

where *N* is the number of atoms in the system, r_i is the position of atom, *i*, and r_i^{ideal} is the ideal position of atom, in the crystal containing the corresponding dislocation. This setup is designed to exclude the distortion caused by the dislocation insertion itself and primarily focuses on the distortion resulting from changes in the atomic environment.

Waviness parameters. We use waviness parameters to represent the degree of a dislocation curvature. The waviness parameters are calculated using the following equation,

$$\frac{1}{N}\sum_{i=1}^{N}|s_i - \bar{s}| \tag{7}$$

where s_i is the position of the dislocation atom, and $\bar{s}$ is the average position of all dislocation atoms.

SRO parameters. The formula for calculating the SRO parameters of the first coordination shell is:

$$\alpha^{ij} = \frac{P^{ij} - c^j}{\delta^{ij} - c^j} \tag{8}$$

where P^{ij} is the probability of finding an atom of type, *i*, in the first coordination shell of an atom of type *j*, c^j is the concentration of an atom, *j*, and δ^{ij} is the Kronecker delta function:

$$\delta_{ij} = \begin{cases} 1 & i = j, \\ 0 & i \neq j. \end{cases} \tag{9}$$

For paired atoms of the same species, a positive SRO parameter indicates a tendency to approach each other, while a negative parameter indicates the opposite. For paired atoms of different species, the trend is reversed, with a positive SRO parameter indicating repulsion and a negative parameter indicating aggregation.

Partitioning strategy

To facilitate the study of elemental aggregation in the local environment, the original system was divided into distinct regions for the calculation of local elemental concentrations, SRO parameters, and stress distributions. A schematic of the initial system and the partitioning strategy is presented in Fig. 11.

Between dislocations. To capture the local atomic environment between dislocations, the simulation box was divided into 12 layers along the *Y*-axis, each with a thickness of approximately 10 Å, with dislocations positioned between layers 3 and 4, as well as between layers 9 and 10, respectively. A similar partitioning method is applied along the *X*-axis. While screw dislocations are introduced as quadrupoles, only one pair of

dipoles is considered in the analysis due to the symmetry. For instance, when analyzing along the *Y*-axis, only the region within the green line is considered; along the *X*-axis, only the region within the yellow line is included. In the edge-dislocation model, position, A, corresponds to the side of the extra half-plane, while position, B, represents the missing half-plane. In the screw-dislocation model, positions, A, B, C, and D, denote different locations between screw dislocations of opposite helicities. Our subsequent results indicate that these positions are not equivalent.

Near dislocations. To characterize the atomic environment near the dislocation core, we define an annular cylindrical region centered on the dislocation line, as shown in Fig. 11c. Since the dislocation may become wavy during the simulation, the average position of the dislocation was used as the axis of the cylinder.

Data availability

All data generated, used, and/or analyzed during the current study are available on request from Xiang-Guo Li (lixguo@mail.sysu.edu.cn). The MTP potential and its training data have been published in an open repository (https://github.com/ucsdlxg/CrMoNbTaVW-ML-interatomic-model).

Code availability

The DFT calculations were performed with the Vienna ab initio simulation package. The training of MTP potential used the MAML (Materials machine learning) package. The LAMMPS package was used to perform MD/MC simulations. All the other codes that support the findings of this study are available from Xiang-Guo Li (lixguo@mail.sysu.edu.cn) upon reasonable request.

Received: 19 October 2025; Accepted: 6 February 2026;
Published online: 19 February 2026

References

1. Yeh, J.-W. et al. Nanostructured high-entropy alloys with multiple principal elements: novel alloy design concepts and outcomes. *Adv. Eng. Mater.* **6**, 299–303 (2004).
2. Cantor, B., Chang, I. T. H., Knight, P. & Vincent, A. J. B. Microstructural development in equiatomic multicomponent alloys. *Mater. Sci. Eng. A* **375–377**, 213–218 (2004).
3. Senkov, O. N., Wilks, G. B., Miracle, D. B., Chuang, C. P. & Liaw, P. K. Refractory high-entropy alloys. *Intermetallics* **18**, 1758–1765 (2010).
4. Senkov, O. N., Miracle, D. B., Chaput, K. J. & Couzinie, J.-P. Development and exploration of refractory high entropy alloys—A review. *J. Mater. Res.* **33**, 3092–3128 (2018).
5. Senkov, O. N., Wilks, G. B., Scott, J. M. & Miracle, D. B. Mechanical properties of $Nb_{25}Mo_{25}Ta_{25}W_{25}$ and $V_{20}Nb_{20}Mo_{20}Ta_{20}W_{20}$ refractory high entropy alloys. *Intermetallics* **19**, 698–706 (2011).
6. Maresca, F. & Curtin, W. A. Mechanistic origin of high strength in refractory BCC high entropy alloys up to 1900K. *Acta Mater.* **182**, 235–249 (2020).
7. Yin, S. et al. Atomistic simulations of dislocation mobility in refractory high-entropy alloys and the effect of chemical short-range order. *Nat. Commun.* **12**, 4873 (2021).
8. Ji, W. & Wu, M. S. Retainable short-range order effects on the strength and toughness of NbMoTaW refractory high-entropy alloys. *Intermetallics* **150**, 107707 (2022).
9. Wang, X., Maresca, F. & Cao, P. The hierarchical energy landscape of screw dislocation motion in refractory high-entropy alloys. *Acta Mater.* **234**, 118022 (2022).
10. Chen, S. et al. Short-range ordering alters the dislocation nucleation and propagation in refractory high-entropy alloys. *Mater. Today* **65**, 14–25 (2023).
11. Zhang, F. X. et al. Local structure and short-range order in a NiCoCr solid solution alloy. *Phys. Rev. Lett.* **118**, 205501 (2017).
12. Zhang, R. et al. Short-range order and its impact on the CrCoNi medium-entropy alloy. *Nature* **581**, 283–287 (2020).
13. Han, Y. et al. Ubiquitous short-range order in multi-principal element alloys. *Nat. Commun.* **15**, 6486 (2024).
14. Chen, X. et al. Direct observation of chemical short-range order in a medium-entropy alloy. *Nature* **592**, 712–716 (2021).
15. Fantin, A., Manzoni, A. M., Springer, H., Kamachali, R. D. & Maaß, R. Local lattice distortions and chemical short-range order in MoNbTaW. *Mater. Res. Lett.* **12**, 346–354 (2024).
16. Luo, X. et al. Correlations between local chemical fluctuations and grain boundary strength in Ti-Zr-Nb-Ta-Mo refractory multi-principal element alloys. *Scr. Mater.* **256**, 116438 (2025).
17. Wu, C.-Y. et al. Observation of short-range order in refractory high-entropy alloys from atomic-positions deviation using stem and atomistic simulations. *Mater. Today Phys.* **57**, 101796 (2025).
18. Frey, C., Silverstein, R. & Pollock, T. M. A high stability B2-containing refractory multi-principal element alloy. *Acta Mater.* **229**, 117767 (2022).
19. Yin, B., Yoshida, S., Tsuji, N. & Curtin, W. A. Yield strength and misfit volumes of NiCoCr and implications for short-range-order. *Nat. Commun.* **11**, 2507 (2020).
20. Li, L. et al. Evolution of short-range order and its effects on the plastic deformation behavior of single crystals of the equiatomic Cr-Co-Ni medium-entropy alloy. *Acta Mater.* **243**, 118537 (2023).
21. Hsiao, H.-W. et al. Data-driven electron-diffraction approach reveals local short-range ordering in CrCoNi with ordering effects. *Nat. Commun.* **13**, 6651 (2022).
22. Wu, Y. et al. Short-range ordering and its effects on mechanical properties of high-entropy alloys. *J. Mater. Sci. Technol.* **62**, 214–220 (2021).
23. Wang, L. et al. Tailoring planar slip to achieve pure metal-like ductility in body-centred-cubic multi-principal element alloys. *Nat. Mater.* **22**, 950–957 (2023).
24. Wang, T. et al. Unraveling dislocation-based strengthening in refractory multi-principal element alloys. *npj Comput. Mater.* **10**, 143 (2024).
25. Hsu, W.-C., Shen, T.-E., Liang, Y.-C., Yeh, J.-W. & Tsai, C.-W. In situ analysis of the Portevin-Le Chatelier effect from low to high-entropy alloy in equal HfNbTaTiZr system. *Acta Mater.* **253**, 118981 (2023).
26. Xia, Y., Lyu, S., Li, W., Chen, Y. & Ngan, A. H. Defect-induced inhomogeneous atomic environments in complex concentrated alloys. *Int. J. Plast.* **169**, 103719 (2023).
27. Wang, B. et al. High-temperature deformation behavior and microstructural evolution of NbZrTiTa refractory high entropy alloy. *J. Alloy. Compd.* **936**, 168059 (2023).
28. Tsai, C.-W. et al. Portevin-Le Chatelier mechanism in face-centered-cubic metallic alloys from low to high entropy. *Int. J. Plast.* **122**, 212–224 (2019).
29. Mu, Y. et al. A high-entropy alloy with dislocation-precipitate skeleton for ultrastrength and ductility. *Acta Mater.* **232**, 117975 (2022).
30. Guo, B. et al. Segregation-dislocation self-organized structures ductilize a work-hardened medium entropy alloy. *Nat. Commun.* **16**, 1475 (2025).
31. Li, X.-G. et al. Quantum-accurate spectral neighbor analysis potential models for Ni-Mo binary alloys and fcc metals. *Phys. Rev. B* **98**, 094104 (2018).
32. Li, X.-G., Chen, C., Zheng, H., Zuo, Y. & Ong, S. P. Complex strengthening mechanisms in the NbMoTaW multi-principal element alloy. *npj Comput. Mater.* **6**, 1–10 (2020).
33. Dai, F.-Z., Sun, Y., Wen, B., Xiang, H. & Zhou, Y. Temperature dependent thermal and elastic properties of high entropy $(Ti_{0.2}Zr_{0.2}Hf_{0.2}Nb_{0.2}Ta_{0.2})B_2$: Molecular dynamics simulation by deep learning potential. *J. Mater. Sci. Technol.* **72**, 8–15 (2021).
34. Byggmästar, J., Nordlund, K. & Djurabekova, F. Simple machine-learned interatomic potentials for complex alloys. *Phys. Rev. Mater.* **6**, 083801 (2022).

35. Xiao, Y. et al. Microstructure and oxidation behavior of the CrMoNbTaV high-entropy alloy. *J. Mater. Res.* **34**, 301–308 (2019).
36. Long, Y., Liang, X., Su, K., Peng, H. & Li, X. A fine-grained NbMoTaWVCr refractory high-entropy alloy with ultra-high strength: microstructural evolution and mechanical properties. *J. Alloy. Compd.* **780**, 607–617 (2019).
37. Das, S. & Robi, P. S. A novel refractory WMoVCrTa high-entropy alloy possessing fine combination of compressive stress-strain and high hardness properties. *Adv. Powder Technol.* **31**, 4619–4631 (2020).
38. Fu, X., Li, Y., Hou, C., Lu, H. & Song, X. Phase stability and transition of CrTaVW high-entropy alloy. *J. Alloy. Compd.* **1002**, 175481 (2024).
39. Wang, Z. et al. Recent research progress on the passivation and selective oxidation for the 3d-transition-metal and refractory multi-principal element alloys. *npj Mater. Degrad.* **7**, 86 (2023).
40. Statham, C. D., Koss, D. A. & Christian, J. W. The thermally activated deformation of niobium-molybdenum and niobium-rhenium alloy single crystals. *Philos. Mag. A J. Theor. Exp. Appl. Phys.* **26**, 1089–1103 (1972).
41. Dirras, G. et al. Microstructural investigation of plastically deformed $Ti_{20}Zr_{20}Hf_{20}Nb_{20}Ta_{20}$ high entropy alloy by X-ray diffraction and transmission electron microscopy. *Mater. Charact.* **108**, 1–7 (2015).
42. Lee, C. et al. Strength can be controlled by edge dislocations in refractory high-entropy alloys. *Nat. Commun.* **12**, 5474 (2021).
43. Chen, B. et al. Unusual activated processes controlling dislocation motion in body-centered-cubic high-entropy alloys. *Proc. Natl. Acad. Sci. USA* **117**, 16199–16206 (2020).
44. Zuo, Y. et al. Performance and cost assessment of machine learning interatomic potentials. *J. Phys. Chem. A* **124**, 731–745 (2020).
45. Song, Q., Li, Z., Zhu, Y. & Huang, M. On the interaction of solute atoms with circular inhomogeneity and edge dislocation. *Int. J. Plast.* **111**, 266–287 (2018).
46. Chaussidon, J., Fivel, M. & Rodney, D. The glide of screw dislocations in bcc Fe: atomistic static and dynamic simulations. *Acta Mater.* **54**, 3407–3416 (2006).
47. Zhao, F., Liu, W., Zhang, Y. & Duan, H. The hierarchical energy landscape of edge dislocation glide in refractory high-entropy alloys. *J. Mech. Phys. Solids* **193**, 105887 (2024).
48. Maresca, F. & Curtin, W. A. Theory of screw dislocation strengthening in random BCC alloys from dilute to "High-Entropy" alloys. *Acta Mater.* **182**, 144–162 (2020).
49. Chen, S. Y. et al. Peierls barrier characteristic and anomalous strain hardening provoked by dynamic-strain-aging strengthening in a body-centered-cubic high-entropy alloy. *Mater. Res. Lett.* **7**, 475–481 (2019).
50. Shapeev, A. V. Moment tensor potentials: a class of systematically improvable interatomic potentials. *Multiscale Model. Simul.* **14**, 1153–1173 (2016).
51. de Jong, M. et al. Charting the complete elastic properties of inorganic crystalline compounds. *Sci. Data* **2**, 1–13 (2015).
52. Zunger, A., Wei, S.-H., Ferreira, L. G. & Bernard, J. E. Special quasirandom structures. *Phys. Rev. Lett.* **65**, 353 (1990).
53. Van De Walle, A., Asta, M. & Ceder, G. The alloy theoretic automated toolkit: a user guide. *Calphad* **26**, 539–553 (2002).
54. Hirel, P. Atomsk: a tool for manipulating and converting atomic data files. *Comput. Phys. Commun.* **197**, 212–219 (2015).
55. Thompson, A. P. et al. LAMMPS - a flexible simulation tool for particle-based materials modeling at the atomic, meso, and continuum scales. *Comput. Phys. Commun.* **271**, 108171 (2022).
56. Jian, W.-R., Xu, S. & Beyerlein, I. J. On the significance of model design in atomistic calculations of the Peierls stress in Nb. *Comput. Mater. Sci.* **188**, 110150 (2021).
57. Osetsky, Y. N. & Bacon, D. J. An atomic-level model for studying the dynamics of edge dislocations in metals. *Model. Simul. Mater. Sci. Eng.* **11**, 427 (2003).
58. Jian, W.-R., Xu, S., Su, Y. & Beyerlein, I. J. Role of layer thickness and dislocation distribution in confined layer slip in nanolaminated Nb. *Int. J. Plast.* **152**, 103239 (2022).

Acknowledgements

Xiang-Guo Li would like to acknowledge financial support from the Guangdong Basic and Applied Basic Research Foundation (2025A1515011961), the Fundamental Research Funds for the Central University, Sun Yat-Sen University (24qnpy322), and the Shenzhen Science and Technology Program (Grant No. JCYJ20241202130018024). Xiang-Guo Li, Yuhao Luo, Tianyi Wang and Zhihao Huang also acknowledge the use of computing resources from the Tianhe-2 Supercomputer.

Author contributions

Yuhao Luo: Writing—original draft, Visualization, Formal analysis, Methodology, Investigation, Data curation. Tianyi Wang: Writing— original draft, Visualization, Formal analysis, Methodology, Investigation, Data curation. Zhihao Huang: Visualization, Formal analysis, Methodology, Investigation, Data curation. Yanqing Su: Writing—review & editing, Investigation, Methodology. Shuozhi Xu: Writing— review & editing, Validation, Conceptualization. Peter K. Liaw: Writing—review & editing, Supervision, Resources. Xiang-Guo Li: Writing—review & editing, Funding acquisition, Supervision, Resources, Conceptualization.

Competing interests

Xiang-Guo Li is a guest editor of the npj Computational Materials special collection "Machine Learning Interatomic Potentials in Computational Materials". He was not involved in the journal's review of or decisions related to this manuscript. The other authors declare that they have no financial or non-financial competing interests.

Additional information

Supplementary information The online version contains supplementary material available at https://doi.org/10.1038/s41524-026-02008-x.

Correspondence and requests for materials should be addressed to Peter K. Liaw or Xiang-Guo Li.